Results in Physics 61 (2024) 107746

Contents lists available at ScienceDirect

Results in Physics

journal homepage: www.elsevier.com/locate/rinp

Characterization and the physical properties of nano-sized Bi_2O_3/polymer for energy and high-refractive index applications

Amani Alruwaili [a], Adel M. El Sayed [b],*

[a] Department of Physics, College of Science, Northern Border University, Arar 73222, Saudi Arabia
[b] Physics Department, Faculty of Science, Fayoum University, El-Fayoum 63514, Egypt

ARTICLE INFO

Keywords:
Bi_2O_3
PVP/PVA blend
Energy storage
High-refractive index materials

ABSTRACT

The present work focuses on developing nanocomposites for optoelectronics and energy storage devices leveraging the unique physicochemical features of bismuth (III) oxide (Bi_2O_3) using a polyvinyl pyrrolidone/polyvinyl alcohol matrix (PV(A/P)). Bi_2O_3 nanofillers (NF) and Bi_2O_3/PV(A/P) nanocomposite (NC) films were prepared by facile chemical solution approaches. The X-ray (XRD) data and a transmission electron image revealed that the NF exhibits a monoclinic phase, resembling slightly deformed agglomerated spheres. In the FTIR spectrum, different stretching vibrations of Bi-O-Bi bonds were found, along with their complexation and interaction with the reactive groups in the matrix. The SEM revealed a uniform distribution of Bi_2O_3 NF loading up to 1.5 wt% on the sample's surface. Thermal analyses (TGA and DSC thermograms) were used to study the thermal stability, melting, and decomposition temperatures of the NC films. The dielectric features were studied under frequencies between 2×10^3 and 8×10^6 Hz and heating from 293 to 393 K. The dielectric constant and energy density were increased with Bi_2O_3 NF content. This implies that we can utilize the prepared NC for the fabrication of energy storage devices. The influences of the Bi_2O_3 NF doping level on the transmittance, band gap, Urbach energy, refractive index, conductivity, and other physical parameters were discussed. The modifications induced in the dielectric/optical parameters make the prepared NC films the best candidates for applications requiring a high refractive index, such as optical coatings and integrated photonic devices.

Introduction

Polymer nanocomposites (NC), combinations of biopolymer and nano-sized ceramic or metal oxide, are attracting increasing attention worldwide, owing to ease of fabrication, technological and industrial importance, eco-friendliness, and cost-effectiveness. These multifunctional materials can be used for various purposes, including sensors, drug delivery, radiation shielding, food packaging, water treatment, and micro- and optoelectronic systems [1–3]. These applications can also be extended to include the energy sector (conversion and/or storage), optical coatings, and integrated photonic devices [4,5].

Improving the electrostatic energy that can be stored in dielectric capacitors with high energy density is urgently desired. For this purpose, high dielectric permittivity (ε') and small loss (ε'') are the most promising features [6–8]. To improve the polymer' ε', it should be mixed with fillers with high ε'. Keep in mind that the high filler content can result in a decrease in the composite's processing performance [6]. Deng et al. [7] introduced PbS and graphitic-C_3N_4@PbS into a polymer blend. The ternary composites showed higher ε' and lower ε'' values than the binary ones. In addition, Cr_2C_3/clay/poly(vinylidene fluoride) (PVDF) ternary composite exhibited lower ε' and lower ε'' compared to those of Cr_2C_3/PVDF [6]. Panomsuwan and Manuspiya [8] reported a significant increase in the ε' of the $BaTiO_3$/epoxy composites and low ε'' at a low filler ratio. They attributed their results to the enhanced interfacial polarization combined with the continuous pathways, interconnections, and composite network structure. Doping a carboxymethyl cellulose-based blend with NiO moved the index of refraction from ~1.44 to 2.23 [9]. The synthesis of NC with such a high refractive index has advantageous properties for use in antireflective coatings, photodetectors, light-emitting diodes, and image sensors [4,5].

Among the biopolymers, PVA (polyvinyl alcohol) and PVP (polyvinyl pyrrolidone) are synthetic, water-soluble, optically transparent, biocompatible, biodegradable, non-toxic, and non-carcinogenic polymers [10]. In addition, the flexibility, eco-friendliness, microbial resistance, and self-healing ability make PVA the best choice for various utilizations in the textile, wood, and medicine industries [11].

---

* Corresponding author.
E-mail address: ams06@fayoum.edu.eg (A.M. El Sayed).

https://doi.org/10.1016/j.rinp.2024.107746
Received 2 April 2024; Received in revised form 3 May 2024; Accepted 6 May 2024

Transparent films with enhanced physical properties can be formed by blending PVA and PVP, where the physical interaction between OH (PVA) and C═O (PVP) yields a miscible and homogenous blend solution [10]. Loading NF inside the PV(A/P) blend will certainly improve its performance and widen its uses. FeS/PVA/graphene, SnS/PV(A/P), and CoCuS/PV(A/P) nanocomposites with improved optoelectronic, mechanical, and electrical properties were developed for some industrial and eco-friendly applications and photonic devices [12–15].

In addition to the higher ratio of surface area to volume, the NPs are able to disperse in a uniform manner in the matrix, achieving enhanced density and lower particle-size components [16,17]. Bi_2O_3 is a *p*-type semiconductor with a moderate band gap ($E_g = 2.82$ eV), low cost, high electrochemical stability, refractive index, permittivity, and the least toxic among heavy metal oxides, making it suitable for use as a ceramic nanofiller [11,18,19]. The high Z (83) of Bi and density (8.9 g/cm^3) make it suitable for some biological uses such as imaging (which provides a good contrast) and radio-sensing [20]. It is also preferred over Pb as a γ-ray shield [21]. In this context, Bi-based shielding is used for dose reduction to protect the human breast during tomography [22].

Bi_2O_3 exhibits interesting photoconductivity and photoluminescence, where the incident photons with energies $\geq E_g$ value generate pairs of electron/hole (pair production) and free radicals [11,23]. The high melting point and modulus of Bi_2O_3 introduced good thermal and mechanical stability to the polymer composites [22]. These features pave the way for the use of Bi_2O_3 in optical coatings and optoelectronics, microwave-integrated circuits, Schottky-barrier solar cells, and capacitors [23]. In their study [24], Du et al. prepared (monoclinic) α-, (tetragonal) β-, and α/β- Bi_2O_3 NP by burning the bismuth nitrate in a solution with tartaric acid. The E_g values were 2.9 eV for the α phase, 2.5 eV for β phase, and 2.7 eV for the mixed phase.

Bijanu et al. [10] fabricated BiOCl/PVP/PVA composites as X-ray shields. PVA-Bi_2O_3/carbon nanodot composites were developed for some optoelectronic applications [11]. PVA hydrogel mixed with 20 wt % Bi_2O_3 NPs showed interesting self-healing ability and an improved mechanical modulus relative to the micro-composites [16]. Karaca [19] fabricated β-Bi_2O_3/$Bi_2O_2CO_3$/polypyrrole (PPy) composites for a high-performance supercapacitor. In addition, Bi_2O_3/Au/chitosan was found suitable for tissue engineering/wound dressing utilization [20]. Mahmoud and Al-Ghamdi [23] studied the IV curves of Bi_2O_3/PVAc and found that the composite conductivity increases and then decreases with temperature, depending on the Bi_2O_3 content and the effect of grain boundaries. Adding 5.0 to 25 % Bi_2O_3 NF to PPy improved its stability and made it better at sensing CO_2 gas [25]. The hydrothermally prepared Bi_2O_3 NPs were more suitable than Bi_2O_3 microparticles for shielding against X-ray radiation [26]. Furthermore, researchers used the co-precipitated Bi_2O_3 nanostructure to create Bi_2O_3/PVC NC, which served as radiation-protective cloths for X-ray attenuation [27]. Şahin et al. [28] researched the thermal and mechanical features of the polyethylene of low-density (LDPE) incorporated with Bi_2O_3. Tommalieh [29] reported the impact of Bi_2O_3 created by the laser ablation inside chitosan/PVA on the ε', ε'' and conductivity of the blend. Darwesh et al. [30] deduced the optical parameters of PVA incorporated with 4–12 wt% Bi_2O_3 NPs.

To the best of the authors' knowledge, there is no complete report on the physical properties of Bi_2O_3/PVA or Bi_2O_3/PV(A/P). The present study aims to leverage the unique physicochemical features of Bi_2O_3 (semiconducting nature, photoconductivity, thermal and mechanical stability, and nontoxicity), while avoiding some shortcomings of Bi_2O_3 (low processability) for fabricating flexible nanocomposites based on PV (A/P) with enhanced physical features. The influence of Bi_2O_3 nanofillers (NF) on the structure, surface morphology, thermal stability, dielectric permittivity, and energy density of these NCs are reported. Additionally, the optical features and the values of various optical parameters are determined. The results indicate the possibility of widening the utilization of PV(A/P) blend to include energy storage and applications requiring materials with a high refractive index.

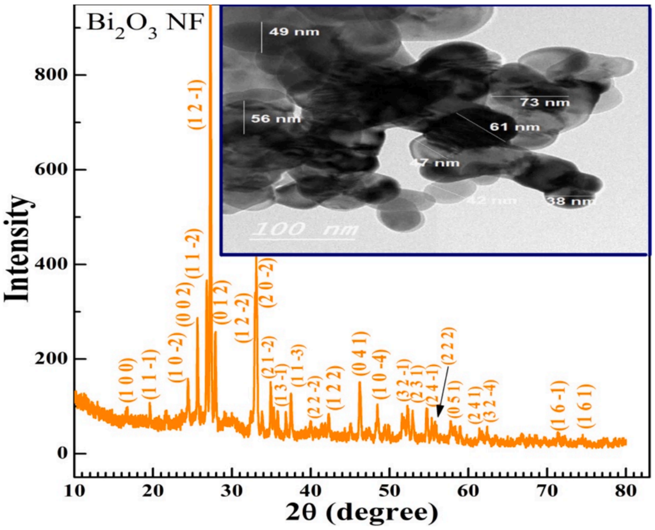

Fig. 1. Bi_2O_3 Powder characterization (XRD pattern and TEM image (inset)).

Preparation of Bi_2O_3/PV(A/P) NC, and measurements

Materials and method

Bismuth (III) nitrate [$(NO_3)_3Bi{\cdot}5H_2O$, 485.07 g/mol, purity ≥ 98 %, Merck] and citric acid [$C_6H_8O_7$, 192.12 g/mol, Merck] were used to prepare Bi_2O_3. Hydrolyzed PVA powder [$[C_2H_3(OH)]_n$, 89,000 g/mol, Acros Organics] and PVP [$(C_6NH_9O)_n$, k 30, 40,000 g/mol, Acros Organics] were used to prepare the PV(A/P) blend. These polymers were dissolved in Double-distilled water (DDW).

$(NO_3)_3Bi$ (3.0 g) in 50 mL of HNO_3 to dissolve and then modified by adding $C_6H_8O_7$ in an equal molar ratio. The mixture was heated at 100 °C to form a yellowish gel which then decomposed to Bi_2O_3 at 450 °C in air. PVA ($\frac{3}{4}$ g) in 50 mL DDW and dissolved by stirring at 85 °C for more than 1.0 h. PVP ($\frac{1}{4}$ g) in 20 mL DDW to dissolve at room temperature (RT). The blend solution was formed by mixing PVA and PVP solutions at RT. The NC were prepared by dispersing a certain amount of Bi_2O_3 in 20 mL DDW using an ultrasound sonicator and then mixed into the blend solution under stirring until a uniform distribution of the fillers was achieved. 0.5, 1.0, 1.5 and 3.0 wt% Bi_2O_3 were added using the equation: $x(\text{wt}\%) = \frac{W_{Bi_2O_3}}{W_{Bi_2O_3}+W_{blend}} \times 100(\%)$, where W denotes the weight. The PV(A/P) blend and NC mixtures were cast in Petri dishes 11 cm in diameter. The dishes were left at RT for more than 10 days until solid films were formed. The free-standing films were then dried at 40 °C in an air oven for 4.0 h, and then characterized. The names of the obtained samples were abbreviated to PV(A/P), 0.5 wt B/b, 1.0 wt% B/b, 1.5 wt% B/b and 3.0 wt% B/b, respectively.

Characterization and measurements

The crystallite (particle) size, structure, and shape of Bi_2O_3 and diffraction in the films were studied using RIGAKU Smart Lab. diffractometer, applying 40-kV and 30-mA. The measurements were done from 5 to 80° on the 2θ scale with 0.01° step width. The used K_α emission line (Cu source) has a wavelength $\lambda = 0.15418$ nm. And JEM 2100, Jeol (Japan), TEM (transmission electron microscopy). The spectrum of FTIR (Fourier-transform infrared) of each film was recorded in the wavenumber range of 4000–400 cm^{-1} using a Bruker/vertex-70/ spectrophotometer attached to a unit to attenuate the total reflection. The Bi_2O_3 distribution on the films' surface was checked using SEM (scanning-electron microscopy) of the Carl-ZEISS/Sigma/500 VP, operated at a 20-kV *e*-beam. The thickness of each film was determined by an accurate micrometer (digital). The TGA/DSC thermal analyses

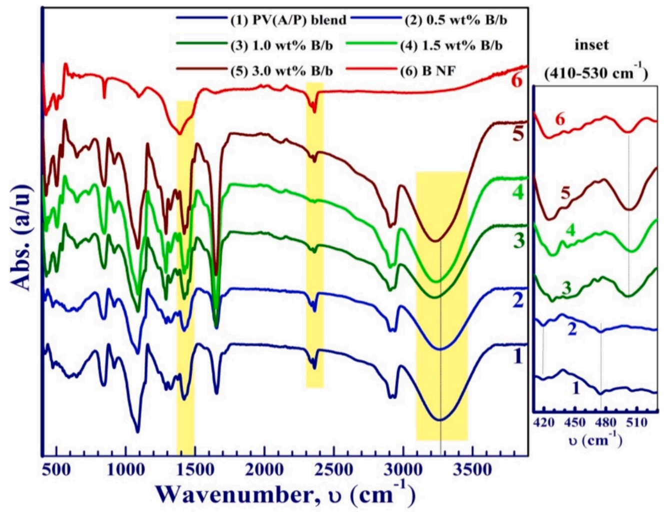

Fig. 2. FTIR spectrum of α-Bi_2O_3 (B NF), PV(A/P) blend (b), and 0.5–3.0 wt% Bi_2O_3/blend.

were performed in 30–550 °C using Perkin-Elmer/STA-6000 in a nitrogen gas flow. The dielectric constant, loss, and energy–density of the films were determined and calculated using the meter bridge (LCR) model HIOKI/IM3536. The C_p accuracy is in the order of 1×10^{-4} pF. The applied frequencies ranged from 2×10^3 to 8×10^6 Hz and heating from 293 to 393 K. Transmittance, reflectance, and absorption spectra in (UV–vis-NIR) were collected using a JASCO-630/spectrophotometer at 200–1500 nm wavelengths.

Results and discussion

Bi_2O_3 features

The phase, crystallite size (Cs), and morphology of the as-prepared Bi_2O_3 were evaluated using the XRD pattern and TEM image shown in Fig. 1. As seen, many (Bragg) diffraction peaks are detected in the 2θ range of 16.44–74.39°. All corresponding peaks have their Miller ($h\ k\ l$) indices inserted on them. The obtained diffraction pattern indicates the formation of α-Bi_2O_3 with monoclinic form, space group (S.G) $P21/c$, and lattice cell parameters (Å); $a = 5.850$, $b = 8.168$, $c = 7.512$. Also, $\alpha = \gamma = 90°$ and $\beta = 113°$. This result is in agreement with DB card no. 9012546 and JCPDS No: 76-1730. In addition, identical lattice parameter values were deduced for the chemically prepared Bi_2O_3 nanoparticles [21]. The size of Bi_2O_3 crystals (Cs) was determined using the Scherrer formula, and its values = 51 ± 8 nm. The inset (TEM image) indicates that the prepared Bi_2O_3 is composed of particles that seem like slightly deformed spheres with a certain agglomeration degree, having sizes in the range of 38–73 nm (the average = 52.3 nm). Similarly, XRD and TEM analyses for the solvothermal-prepared Bi_2O_3 were 30–40 and 34 nm, respectively [28]. Ahamed et al. [18] prepared pure and 3.0 % Zn-doped Bi_2O_3 NPs using a co-precipitation method, with Cs = 67 and 54 nm and grain sizes of 71 and 51 nm, respectively. Kavgaci and Eskalen [11] prepared Bi_2O_3 in the form of microrods (9.72–2.48 μm in length, 0.45 μm in diameter) by the sonochemical method. The sharp and intense diffraction peaks in Fig. 1 demonstrate the high crystallinity and purity of the prepared Bi_2O_3. These results confirm that we have applied a suitable synthetic method to obtain Bi_2O_3 NPs with reasonable size and shape.

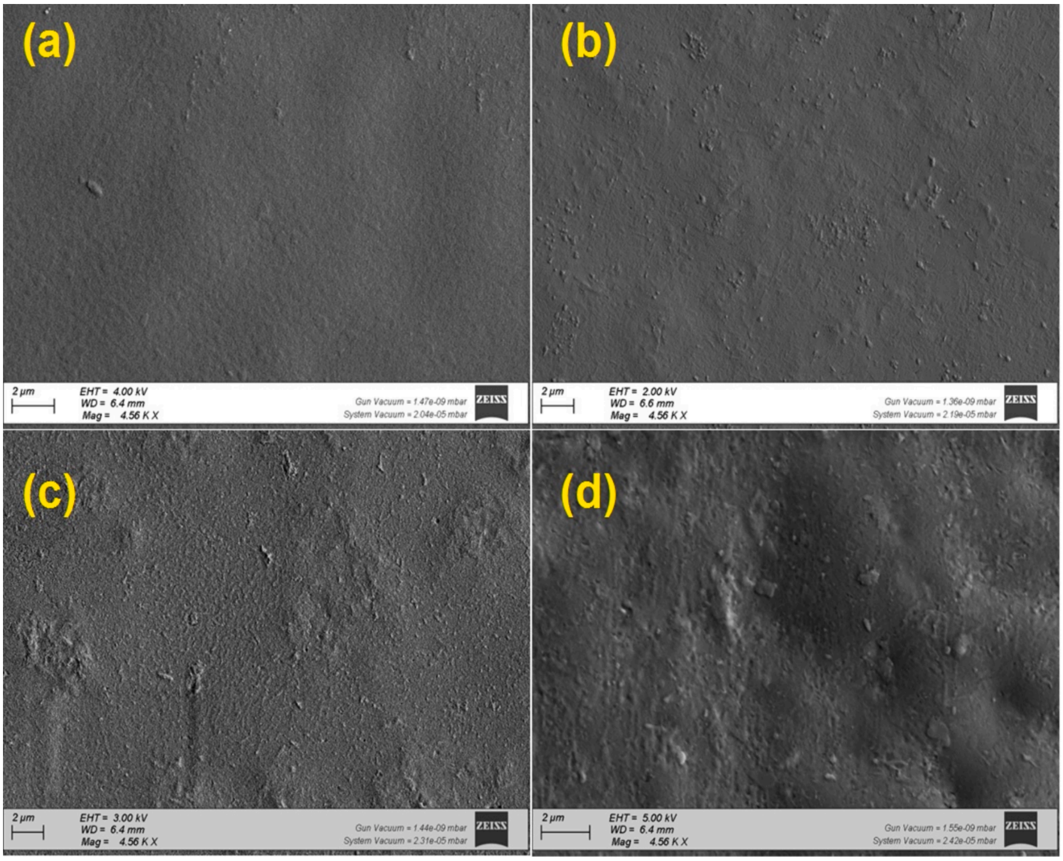

Fig. 3. Micrographs taken by FE-SEM for (a) blend, (b-d) 1.0–3.0 wt% B/b.

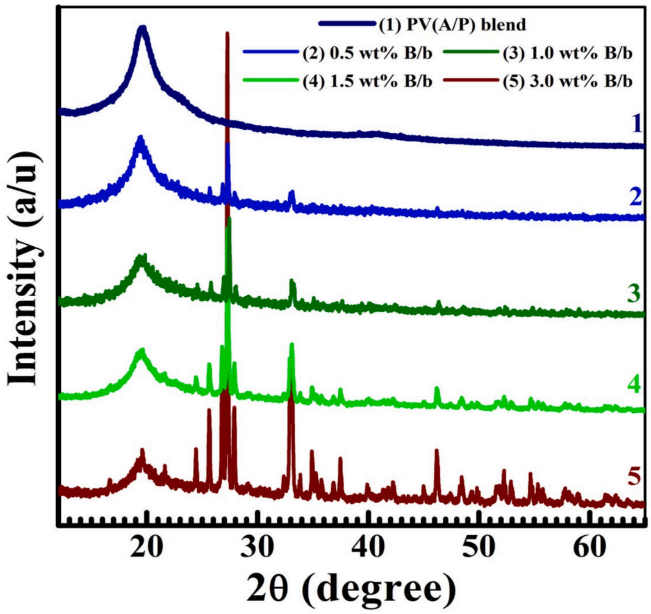

Fig. 4. XRD spectrum of blend and α-Bi_2O_3 /blend NC.

The structural analyses of NC films

FT-IR spectroscopy was used as a powerful technique to check the materials' reactive groups and study the complexation and physical/chemical interactions that govern the NC's features. The spectrum of Bi_2O_3 (shown in Fig. 2) reveals several peaks at 425, 502 (see the inset of this figure), 845, and 1397 cm^{-1}. These peaks arose due to Bi–O and Bi–O–Bi stretching vibrations [17,20,21,28]. In addition, the small band at 1100 cm^{-1} arose due to the OH normal stretching vibration of H_2O that can be adsorbed on the Bi–O lattice [28]. Bijanu et al. [10] found that the O–Bi stretching occurs at 560 cm^{-1}. Eyssa et al. [17] detected two bands at 450 and 1396 cm^{-1} for the O–Bi stretching vibration, and a third peak at 624 cm^{-1} arose from Bi–O–Bi chemical bond vibration in the Bi_2O_3 spectrum.

The PV(A/P) spectrum consists of many absorption peaks; the widest one at 3280 cm^{-1} is assigned to the O–H stretching of PVA. The C–H symmetric and asymmetric stretching is seen at 2900–2920 cm^{-1} [16]. The stretching of C═O (PVA′ vinyl acetate) is represented by a sharp peak at 1630 cm^{-1}. C–H bond bending appears at 1420 cm^{-1}. A tiny band at 1300 cm^{-1} is attributed to the vibrations of the (OH + CH). The C–O–C bond (PVA' acetyl group) stretching makes a strong band at ~1090 cm^{-1}. In addition, CH_2 bending arose at 849 cm^{-1} [31]. A small band of very low intensity can be seen at 650 cm^{-1} and could be attributed to NH vibration [32].

Investigating the spectra of Bi_2O_3/blend NC leads to the following notes: *i*) No new peaks can be seen in the Bi_2O_3/blend spectra, which indicates the interaction of Bi_2O_3 with the matrix's reactive groups throughout forming hydrogen bonds and/or Van der Waals attraction, *i. e.*, physical interaction. *ii*) The intensity, wideness, and central position of the O–H band changed after loading Bi_2O_3 NF. The physical interactions of OH PVA's groups with the Bi_2O_3 NF originate from the great tendency of OH groups to form charge transfer complexes with Bi–O through chelation, and the reinforcing effect of Bi_2O_3 [16,28]. *iv*) The $Bi_2O_3{}'$ absorption peaks at 425 and 502 cm^{-1} appear in the 1.0 wt% Bi_2O_3/blend and their intensities increase with raising Bi_2O_3 content. Similarly, the incorporation of Bi_2O_3 in the Au/chitosan matrix induced new peaks at 622 and 529 cm^{-1} assigned to the Bi-O bond [20]. *v*) The intensity of most peaks decreases at first to 1.5 wt% Bi_2O_3 content and then increases at 3.0 wt%, whereas the height of the two bands at 650 and 1300 cm^{-1} significantly increases with filler content. These results confirm the strong interaction and complexation between Bi_2O_3 and the blend chains.

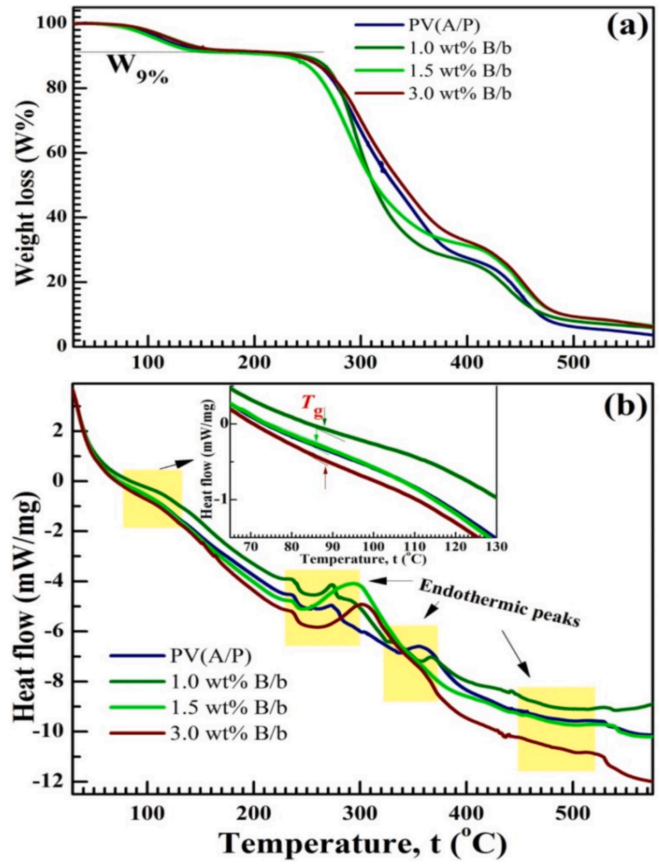

Fig. 5. (a) TGA and (b) DSC thermograms of PV(A/P) and Bi_2O_3/blend films.

Fig. 3(a–d) displays the surface morphology and filler distribution on the blend surface. The PV(A/P) blend exhibits a crack-free, homogenous, and nonporous surface. This confirms that PVA and PVP polymers are well-miscible and biocompatible with each other. The 1.0 and 1.5 wt % Bi_2O_3 NF are uniformly distributed, and the film surface acquired some roughness. At 3.0 wt% filler ratio, the Bi_2O_3 tends to agglomerate, forming some clusters, and the roughness increases significantly. XRD patterns of the obtained films are depicted in Fig. 4. The chart of the unfilled matrix indicates its semicrystalline structure, where the pattern contains two peaks located at 19.7° (the major peak) and a minor one at 40.5° which are assigned to the (Bragg) peak of the PV(A/P) blend. The strong peak arose from PVA (1 0 1) planes and d-spacing of 0.45–0.5 nm [33]. The forces of hydrogen bonding cause the blend molecules and chains to be arranged in lamellas distributed inside amorphous parts [34]. Almost the same note was reported for the sodium alginate/PVA blend [35]. Upon loading Bi_2O_3 NF, the intensity of these two peaks greatly decreased without any observed shift in their positions, and the Bi_2O_3 main peaks (Fig. 1) are seen with increasing intensity with increasing Bi_2O_3 NF content. Similarly, XRD charts of PEO/PVA contained signals related to the MWCNTs/ZnO fillers [36]. This result again confirms the incorporation of Bi_2O_3 NF inside the PV(A/P) matrix and that these NF deteriorate the ordered structures (crystalline lamellas) and improve the amorphousity. In conclusion, the structure of PV(A/P) is modified upon doping with Bi_2O_3, and it is expected that the composite's conductivity will be better [35].

Thermal (TGA and DSC) analyses

To check the films' thermal stability, the loss of weight (W%) with heating (TGA thermograms) in the 30–550 °C temperature range is

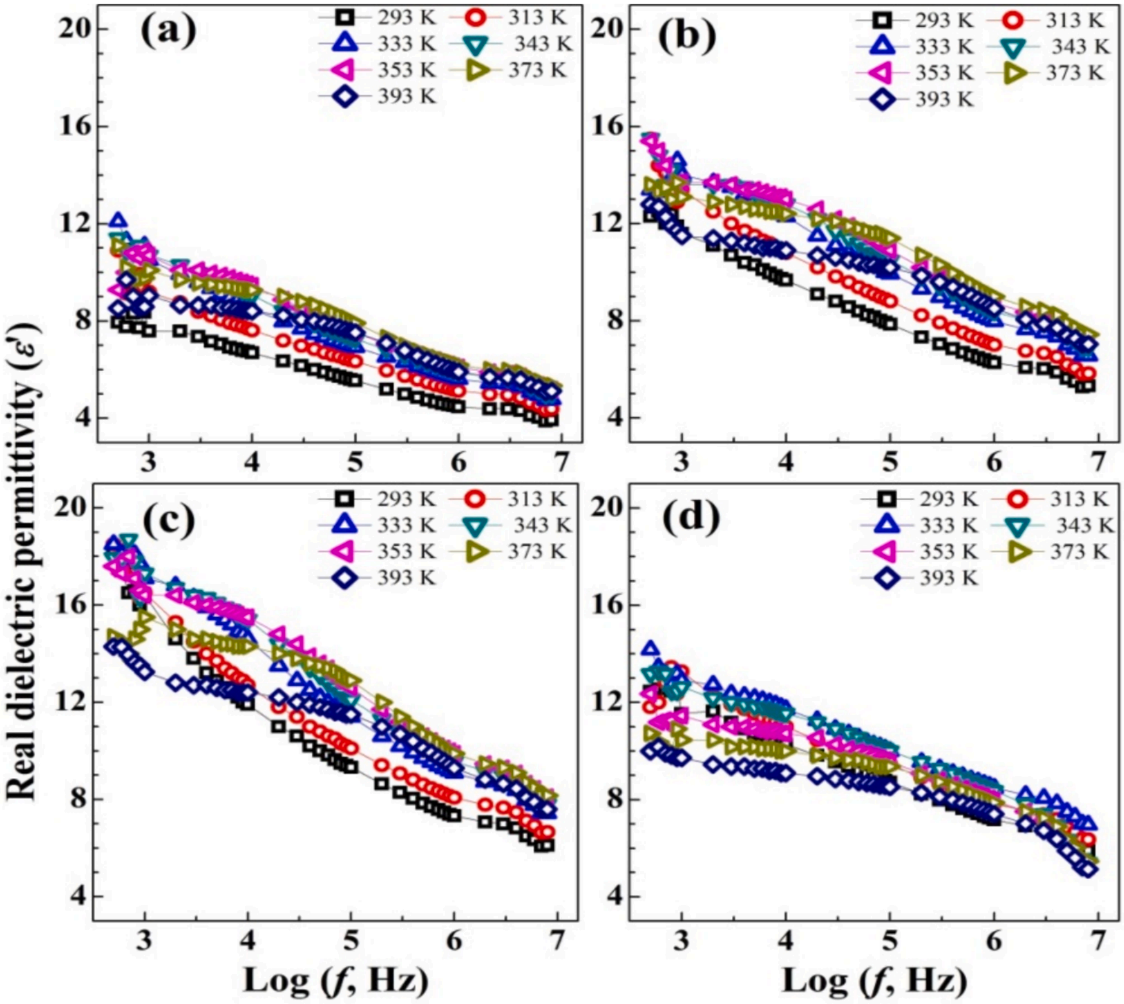

Fig. 6. (a–d): Dielectric constant (ε′) dependent on frequency at some selected temperatures for PV(A/P), 1.0, 1.5 and 3.0 wt% B/b.

shown in Fig. 5(a). The W% can be divided into three steps. The initial one represents a W% of about 9 % for the films at a temperature$T_{9\%} = 150\ ^\circ C$, owing to the moisture (or residual water) and CO/CO_2 removal that were adsorbed from the surrounding environment [37]. In the temperature range of 150–240 °C the W% is constant, *i.e.*, the blend and 3.0 wt% B/b films are thermally stable till 240 °C. The 1.5 wt% B/b film showed thermal stability till 230 °C (the onset decomposition temperature). Therefore, all films have thermal stability in the range of 30–230 °C, which is suitable for practical and industrial applications including electrochemical and optoelectronic devices. The 2^{ed} (main) decomposition occurs in the range 240–385 °C for the blend and 3.0 wt % B/b, where the W% = 70 % and 66 %, respectively. The stage extends to 370 °C only for 1.0 and 1.5 wt% B/b films. This W% arose due to the degradation of blend chains, especially those of PVP (reduced molecular weight and blend backbone cleavage). The 3^{ed} stage of W% takes place at T ~ 408 °C for the blend, 400 °C for 1.0 wt% B/b, and 425 °C for the 1.5 and 3.0 wt% B/b. This stage originates from PVA chain decomposition [38]. The final remaining weight of about 4–10 % is the charcoal, where its weight is increased with Bi_2O_3 NF content. Similar TGA thermograms were obtained for the chitosan/PVA blend prepared by solution casting and electrospinning [39,40].

Fig. 5(b) displays the differential scanning calorimetry thermograms (DSC curves). The melting of the blend produces an endothermic peak in the temperature range of 230–300 °C originates due to the melting of the blend. Other endothermic peaks at 325–370 °C and 450–520 °C occurred due to the full decomposition of PVA. The literature confirms that PVA undergoes multi-stage decomposition at 330, 430, and 450 °C [41]. Bijanu et al. [42] saw the 1st endothermic peak in the DSC spectrum of PVA (50 %)/PVP (50 %) in the range of 130–150 °C. There is no endothermic peak before 230 °C due to the difference in our blend structure (75 % PVA and 25 % PVP). The inset of Fig. 5(b) shows the glass (T_g) transition temperature. The T_g of the blend and 1.5 wt% B/b is about 85 °C and this is consistent with the literature, where T_g of PVA is about 86 °C [43]. The 1.0 and 3.0 wt% B/b exhibit a slight increase in T_g reaching 88 °C. The glass → rubber transition, which arises due to the gained thermal energy, enhances the chains' micro-Brownian motion and segments of the blend. The slight improvements in T_g at 3.0 wt% filler content are due to the fact that the NC films are more compact and denser, which restricts chain mobility [44].

Dielectric properties

The frequency (*f*)-relying of the ε' and ε'' components of ε^* (the complex permittivity, $\varepsilon^* = \varepsilon' + j\varepsilon''$) are shown in Figs. 6 and 7. The ε' refers to the polarization contribution, and is related to the energy storage ability, while ε'' refers to the energy loss. Fig. 6(a–d) and Fig. S1 (a–d) show the ε' of PV(A/P) blend and 1.0, 1.5 and 3.0 wt% Bi_2O_3/blend in the *f* range of 2×10^3 Hz–8.0×10^6 Hz at some selected temperatures (293–393 K). Although the temperature has a decisive effect, the values of ε' depend primarily on *f*. At each temperature, the ε' value is high owing to the charge accumulation beside the electrodes. The small *f* gives enough time for the charge's response to the directional change of

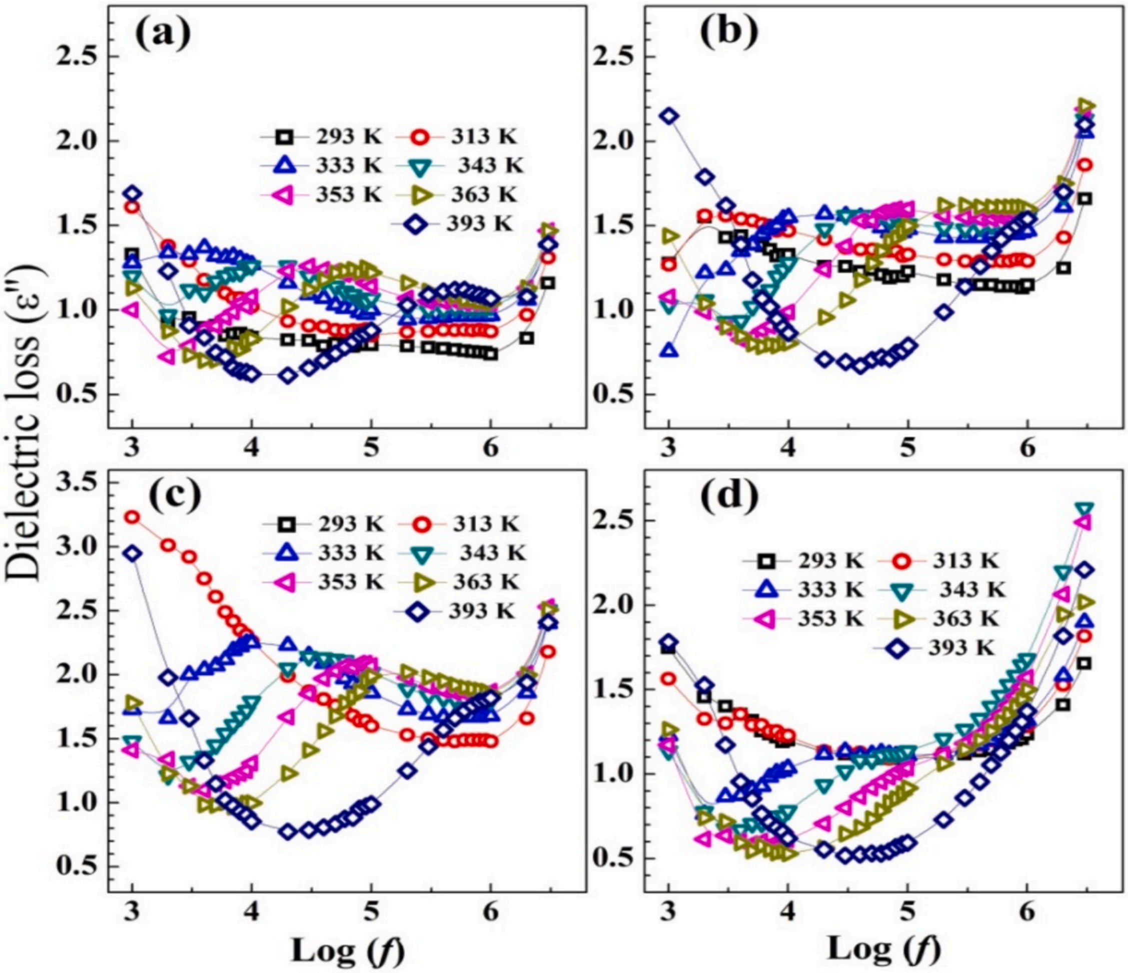

Fig. 7. (a–d): Dielectric loss (ε'')-dependent on f at some selected temperatures for PV(A/P), 1.0, 1.5 and 3.0 wt% B/b.

the electric field. As f increases, the ε' value decreases, because the dipoles don't have enough time to align themselves with the fast reversal electric field, which reduces the contribution of dipole polarization [45,46]. Fig. S1(a–d) shows that the values of ε' increase with raising the temperature of the blend to 343 K and then decrease with further heating. This relaxation peak, called the α_c–process, shifts to higher temperatures as f increases and indicates the dipolar nature of the dielectric behavior [32]. This α_c–process is related to the main chain' Brownian movement in the amorphous parts.

The 1.0 and 1.5 wt% Bi_2O_3/blend NC exhibit improved ε' values relative to those of the unfilled PV(A/P) blend. The observed ε' values are very high compared with those obtained by Tommalieh [29] for chitosan/PVA blend loaded with Bi_2O_3 NPs. Loading Bi_2O_3 NF certainly enhances the matrix heterogeneity, increases the disorder and defects inside the blend, provides a sufficiently larger surface area, reduces the potential barrier for the de-trapping, and increases the interfacial polarization and hence ε' [47,48]. However, At 3.0 wt% Bi_2O_3 level, the added NF seems to pile up (agglomerate) which may result in a reduction in the interaction zone with the blend and break the formed conductive network at the low doping level. Similar results were reported for Bi_2O_3/LDPE [47], boehmite/carboxymethyl chitosan/cashew gum [49], and TiO_2/MWCNT/CMC/PEO [50], when the filler level exceeded a certain ratio, ε' decreased.

The frequency (f)-dependence of ε'' spectra of the PV(A/P) blend, 1.0, 1.5, and 3.0 wt% Bi_2O_3/b is depicted in Fig. 7(a–d) at temperatures in the range of 293–393 K. The ε'' of the blend, 1.0 and 1.5 wt% Bi_2O_3 is in the range of 0.6–1.7, 0.7–2.2, and 0.8–3.2, respectively. Then, it decreased to be in the range of 0.5–2.6 at 3.0 wt% Bi_2O_3 content. In the middle region of applied f, ε'' seems constant. At temperatures $\geq$ 333 K, the chain motion induces relaxation peaks whose maximum position shifts to a higher f with further heating. The reason may be that the crystalline regions dissolve well inside the amorphous regions when the temperature is raised [41]. The important observation here is that all samples exhibit almost similar ε'' values while increasing Bi_2O_3 content increases the ε'. The dielectric displacement ($D = \varepsilon_o \varepsilon' E$) and energy density ($U_e = \int DdE = \frac{1}{2}\varepsilon_o \varepsilon' E^2$) are proportional to the electric field strength E and ε' [51]. Small or stable ε'' combined with high ε' is technologically desirable for the NC to be utilized for energy storage applications and devices (supercapacitors, electrostriction systems, etc.). [52].

Fig. 8(a–c) shows the calculated U_e for the blend, 1.0 and 1.5 wt% Bi_2O_3/blend films. The maximum U_e value (at 2.0 kHz) is about 5×10^{-2} J/m^3 at 343 K, 6.8×10^{-2} J/m^3 at 343 K, and 8.35×10^{-2} J/m^3 at 343 K for the matrix, 1.0 and 1.5 wt% Bi_2O_3/blend. The U_e values decrease with f and the corresponding maximum value shifts to a higher temperature. Loading a 1.6 wt% Cr_2O_3 NP/ PVA/CMC increased the U_e of the blend by twice [2]. The obtained data illustrates the possible use of 1.5 wt% Bi_2O_3/blend for energy storage devices.

Optical characterization

The UV/vis/NIR transmittance (T), absorption (Abs), and reflectance (R) were collected to study the optical transition and band structure and to determine the optical constant. Fig. 9(a) shows that the PV(A/P) is

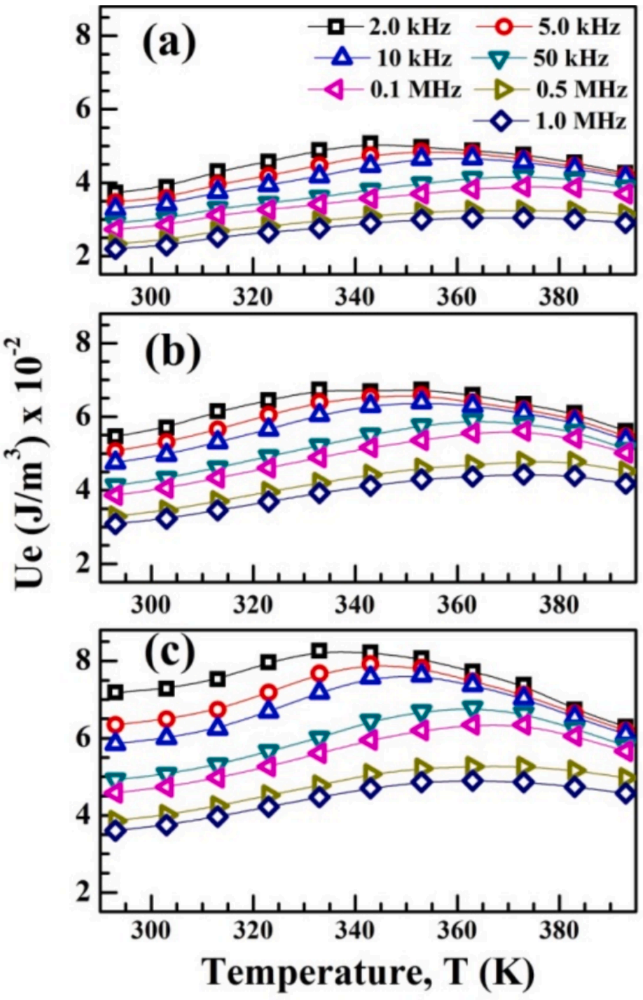

Fig. 8. (a–c): The variation of U_e with the temperature (293–393 K) for PV(A/P) blend, and the blend filled with 1.0 and 1.5 wt% Bi_2O_3 at some selected f.

highly transparent (T ~ 90 %) in the visible and IR regions. 0.5 wt% and 1.0 wt% Bi_2O_3/blend show T in the range of 68–80 % and 24–42 %. The higher filler content makes an opaque blend, where the 3.0 wt% Bi_2O_3 level reduces T to <12 %. A similar result was reported for PVP/PVA (2:3), where 10 wt% CdCuS loading had reduced T% from 81 to 2.0 % [15]. Fig. S2 displays photo images for the samples. The films turn from colorless to yellowish with increasing Bi_2O_3 NF loading. This reflects the role of Bi_2O_3 in hindering the photons from crossing the blend by absorbing and scattering them. The XRD results showed that adding Bi_2O_3 causes defects, disorder, and a reduction in the blend's crystallinity. These factors help to lower T and make the absorption edge wider.

The width of this edge is called the Urbach energy (UE). UE and the coefficient of absorption α are connected by the relation: $\alpha = \alpha_o e^{\left(\frac{h\upsilon - constant}{UE}\right)}$ [30], where $h\upsilon$ is the coming photon energy and α_o is a constant. The parameter α was calculated ($\alpha = abs/thickness$) and the Ln (α) vs. $h\upsilon$ plots are depicted in Fig. 9(b). The α values of the blend increase linearly with $h\upsilon$ and also increase with increasing Bi_2O_3 content. The inset of Fig. 9(b) focuses on the region of the exponential edge and was used to determine the UE value. The slope of each curve in this inset is 1/UE, *i.e.*, UE = 1/[d(Lnα)/dhυ)]. The estimated UE value for the blend is 0.25 eV and increased to 1.13 eV upon loading 1.5 wt% Bi_2O_3. The UE values of all films are listed in Table 1. This increment in UE values confirms the crystallinity decrease seen in XRD results, and defect numbers increase with increasing Bi_2O_3 NF levels [30].

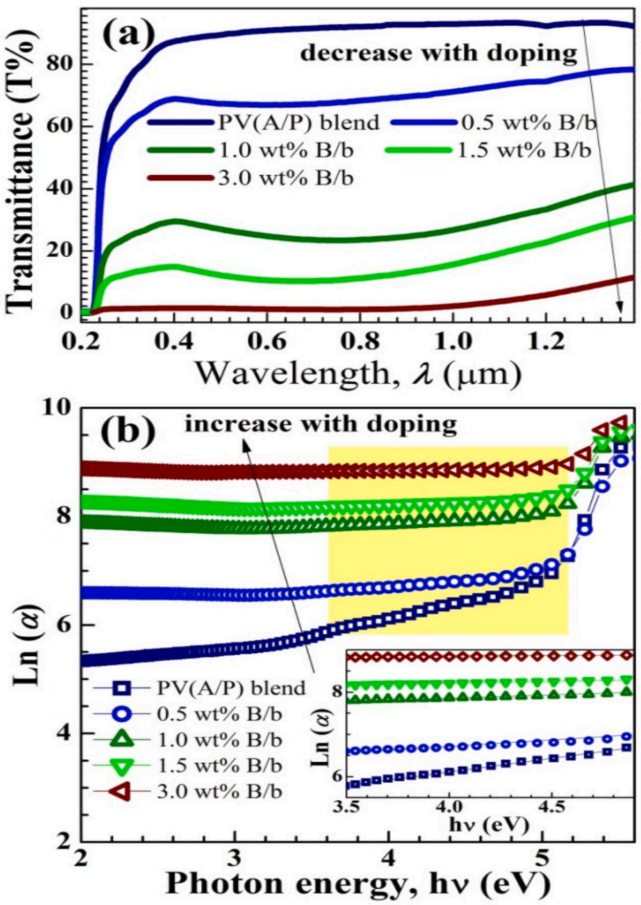

Fig. 9. (a) Transmittance (T) and (b) Ln (α) vs. photon energy for PV(A/P), 1.0, 1.5 and 3.0 wt% Bi_2O_3/blend.

Table 1
Some optical parameters of the samples: Urbach energy (UE), maximum refractive index (n_{max}) and N/m^* ratio.

Sample	UE (eV)	n_{max}	N/m^*/kgm^3
PV(A/P)	0.25	1.3	1.4×10^{55}
0.5 wt% Bi_2O_3	0.48	1.6	2.7×10^{55}
1.0 wt% Bi_2O_3	0.81	3.2	4.8×10^{55}
1.5 wt% Bi_2O_3	1.13	4.6	9.2×10^{55}
3.0 wt% Bi_2O_3	1.35	6.15	17.1×10^{55}

Two of the most essential optical parameters for optoelectronic device design are the refractive (n) and absorption (k) indices. The k index ($k = \frac{\text{Abs} \times \lambda}{\text{thickness} \times 4\pi}$) was calculated (not shown) and used with R spectra to determine the n, where $n = \frac{1+R}{1-R} + \sqrt{\frac{4R}{(1-R)^2} - k^2}$ [9,15]. The recorded R (%) spectra of all films are shown in Fig. S3 (see the Supplementary materials file). Fig. 10(a) displays n vs. λ. The n and R% values of the blend in the vis-NIR wavelengths are ~ 1.3 and <4 %, respectively, and decrease with λ. This behavior of n changed significantly upon loading Bi_2O_3 NF, where n increases gradually and reaches a maximum value of 6.15 with increasing Bi_2O_3 levels 3.0 wt%, and takes on a bell-shaped behavior. Fig. 10(b) shows the almost linear increase of n (at $\lambda = 700$ nm, for comparison) with Bi_2O_3 content. Similarly, filling PVA/graphene films with 10 wt% α-Fe_2O_3 NPs increased n from 1.6 to ~2.65 [53]. According to Darwesh et al. [30] the n value of PVA shifted from 1.2 to only 2.72 at 12 wt% Bi_2O_3 level. Filling the blend with Bi_2O_3 certainly increases the packing density, and the scattering centers inside the matrix, and this makes the NC films more reflective of the coming photons [32].

Another intriguing optical parameter is the ratio (N/m^*), the charge

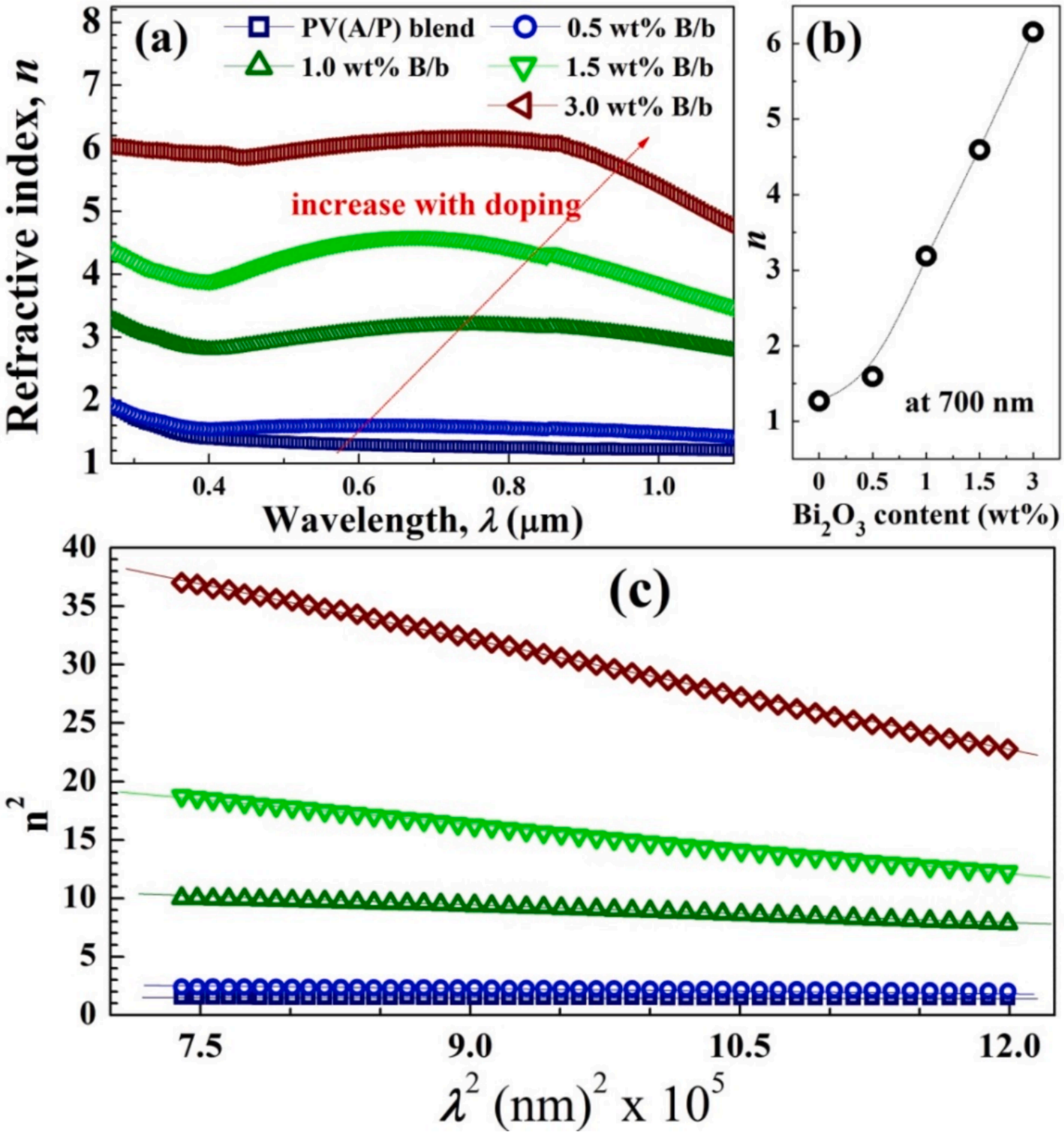

Fig. 10. (a) Refractive index distribution, (b) n dependence on Bi_2O_3 content, and (c) n^2 vsλ^2 to determine (N/m^*) ratio of the PV(A/P), 1.0, and 1.5 wt% Bi_2O_3/blend.

carrier concentration to the electron (e) effective mass. This ratio is contained in the following relation: $n^2 = \varepsilon_L - \lambda^2\left(\frac{Ne^2}{m^*\pi c^2}\right)$, where ε_L and c are constants [12,54]. The ratio (N/m^*) can be determined from the slopes of n^2 andλ^2 plots, as shown in Fig. 10(c). The ratio (N/m^*) of the blend is 1.4 × 10^{55}/kgm^3, and significantly increased to 17.1×10^{55}/kgm^3 at Bi_2O_3 level of 3.0 wt%, see Table 1. Similar results were reported for PV(A/P) modified with SnS NPs [12]. This increase in the carrier concentration is consistent with the crystallinity reduction, seen in XRD data. The literature found a similar note, demonstrating a fourfold increase in the (N/m^*) of PMMA polymer upon 0.25 wt% Cr_2O_3 addition [54]. The PV(A/P) and blend filled with Bi_2O_3 are semicrystalline and can be regarded as direct/indirect bandgap semiconductors [55]. Therefore, it could be useful to shed some light on their allowed direct/indirect transitions. Using the well-known Tauc's relation: $(\alpha \times h\upsilon)^m = (h\upsilon - E_g)A$, where A is a constant, and $m = 0.5/2$ for allowed indirect/direct transitions [56]. Fig. S4(a and b) shows the plots of $(\alpha \times h\nu)^{0.5}$ and $(\alpha \times h\nu)^2$ vs. $h\upsilon$. The E_g values (indirect and direct), as indicated by the arrows, decreased from 5.0 to 4.6 eV and from 5.2 to 5.1 eV. This marginal decrease in E_g was also reported by Şahin et al. [28], for LDPE filled with Bi_2O_3. The E_g of PVA reduced from 5.37 to 5.13 eV [11] upon loading 2.0 wt% Bi_2O_3. Also, loading Bi_2O_3 (5–25 wt%) narrowed the E_g of PPy from 5.0 to 4.3 eV [25].

The impact of the incident photons and Bi_2O_3 doping levels on the conductivity of the blend and NC can be analyzed optically. The conductivity (σ_{optical}) can be estimated from n and α as follows: $\sigma_{\text{optical}} = \frac{n\alpha c}{4\pi}$ [15,57]. Fig. 11 shows the variation of σ_{optical} with $h\upsilon$ and Bi_2O_3 ratios. The 1.0, 1.5, and 3.0 wt% Bi_2O_3 improve σ_{optical} by about two, four, and ten times compared with the pure blend. 1.5 and 3.0 wt% Bi_2O_3 levels induce a peak in the region of 1.5–2.5 eV, and this composition can be

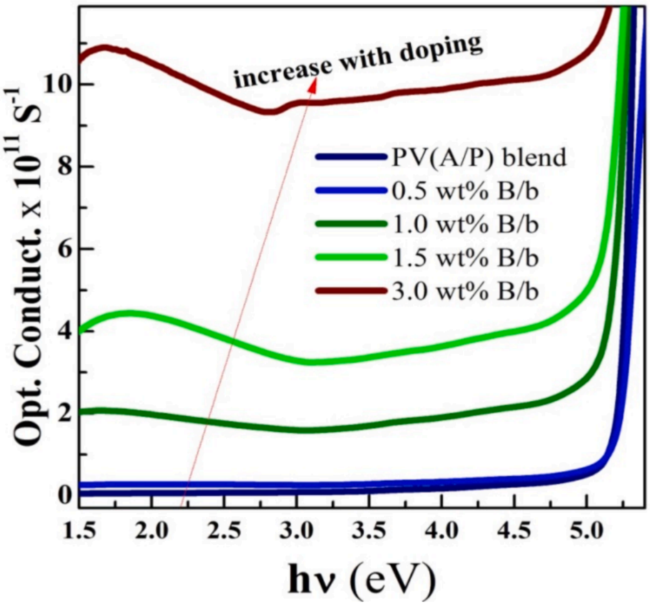

Fig. 11. σ_{optical}-dependence on the photon energy and Bi_2O_3 NF levels.

utilized for optical sensing applications in the visible region. At $h\upsilon \geq$ 4.75 eV ($\lambda \leq$ 260 nm) a sudden increment in σ_{optical} for all films, where the photon in the UV region have the required energy to excite all possible electrons to contribute to the process of conduction [53].

Conclusion

Nano-sized Bi_2O_3 with monoclinic phase and sphere-like morphology, and 0–3.0 wt% Bi_2O_3/PV(A/P) NC films were prepared by facile chemical methods. Bi–O/Bi–O–Bi stretching vibrations appear in the wavenumber range of 425–1397 cm^{-1}. In addition, the physical interaction/complexation between Bi–O and the reactive group of the PV(A/P) matrix (OH, C=O, C–O–C, etc.) were inferred from the changes in the intensity and bands' position. SEM revealed the homogeneity of the blend and the equal and homogenous dispersion of NF on the film surface. XRD results confirm the interaction among the NC film constituents by decreasing the ordered structures in the semicrystalline matrix. TGA&DSC analyses revealed three decomposition stages and three endothermic peaks. The NC films are stable thermally in the range of 30–230 °C and therefore they are suitable for some electrochemical, space, and optoelectronic applications. The ε' and U_e were increased with loading Bi_2O_3 up to 1.5 wt% and displayed relaxation peaks with raising the temperature (heating) from 293 to 393 K. This improvement, combined with the small variation in the dielectric loss, suggests the usability of these NC in energy storage applications. PV(A/P) matrix transparent (90 %) in the visible/IR regions and decreased to 24–42 % at 1.0 wt% Bi_2O_3 level. The UE value moved from 0.25 eV to 1.35 eV at 3.0 wt% filler content, combined with a marginal decrease in the indirect (direct) E_g from 5.0 (5.2) eV to 4.6 (5.1) eV. The interesting result was the increment in n from 1.3 to 6.15 and its bell-shaped distribution. In addition, the (N/m^*) ratio and σ_{optical} enhanced significantly with increasing Bi_2O_3 level. These optical features suggest extending the use of the prepared NC films to include high-n applications such as optical coatings and integrated photonic devices.

CRediT authorship contribution statement

Amani Alruwaili: Writing – review & editing, Writing – original draft, Visualization, Validation, Investigation, Data curation, Conceptualization. **Adel M. El Sayed:** Writing – review & editing, Writing – original draft, Visualization, Validation, Supervision, Software, Resources, Methodology, Investigation, Formal analysis, Data curation, Conceptualization.

Declaration of competing interest

The authors declare that they have no known competing financial interests or personal relationships that could have appeared to influence the work reported in this paper.

Data availability

The datasets used and/or analyzed during the current study available from the corresponding authors on reasonable request.

Acknowledgement

The authors extend their appreciation to the Deanship of Scientific Research at Northern Border University, Arar, KSA for funding this research work through the project number "NBU-FFR-2024-885-02".

Appendix A. Supplementary data

Supplementary data to this article can be found online at https://doi.org/10.1016/j.rinp.2024.107746.

References

[1] El Sayed AM, Alanazi TI. Improving the structural, optical, and electrical properties of carboxymethyl cellulose/starch/selenium oxide nanocomposites for flexible electronic devices. Sci Rep 2024;14:3398. https://doi.org/10.1038/s41598-024-53268-w.

[2] El Sayed AM. Boosting the optical and electrical properties of PVA/Na-CMC blend by Cr_2O_3 nanoparticles for photonic and energy storage applications. J Energy Storage 2024;82:110609. https://doi.org/10.1016/j.est.2024.110609.

[3] Khalifa M, El Sayed AM, Kassem SM, Tarek E. Synthesis, structural, optical, and thermal properties of LaFeO3/Poly(methyl methacrylate)/poly(vinyl acetate) nanocomposites for radiation shielding. Sci Rep 2024;14:3672. https://doi.org/10.1038/s41598-024-54207-5.

[4] Kulshrestha S, Kumari M, Shrivastava AK. Growth and characterization of pure and KDP doped 2-Benzamidoacetic acid organic semiconductor materials for high refractive index devices. Opt Mater 2024;149:114913. https://doi.org/10.1016/j.optmat.2024.114913.

[5] O'Byrne M, Kerzabi B, Abbarchi M, Lifschitz A, Zamora T, Malgras V, Gourdin A, Modaresialam M, Grosso D, Putero M. Investigation of the anatase-to-rutile transition for TiO2 sol-gel coatings with refractive index up to 2.7. Thin Solid Films 2024;790:140193. https://doi.org/10.1016/j.tsf.2023.140193.

[6] Deng Q, Zhou J, Li X, Feng Y, Liang Y, Liu Q. Finely-reconciled high dielectric constant and low dielectric loss in ternary polymer/Cr_2C_3/montmorillonite composite films by filler-synergy strategy. Curr Appl Phys 2021;22:104–10. https://doi.org/10.1016/j.cap.2020.11.006.

[7] Deng Q, Wang J, Chen P, Bo M, Lu Y, Pan Y, et al. Achieving a high dielectric constant and low dielectric loss of polymer composites filled with an interface-bonded g-C_3N_4@PbS narrow-bandgap semiconductor. Coll Surf A 2022;640:128501. https://doi.org/10.1016/j.colsurfa.2022.128501.

[8] Panomsuwan G, Manuspiya H. Enabling high dielectric constant and low loss tangent in $BaTiO_3$–epoxy composites through a 3D interconnected network structure of ceramic phase. J Alloy Compds 2023;953:169968. https://doi.org/10.1016/j.jallcom.2023.169968.

[9] El Sayed AM, Saber S. Structural, optical analysis, and Poole-Frenkel emission in NiO/CMC–PVP: Bio-nanocomposites for optoelectronic applications. J Phys Chem, Solids 163 2022:110590. https://doi.org/10.1016/j.jpcs.2022.110590.

[10] Bijanu A, Rajak G, Paulose R, Arya R, Agrawal V, Gowri VS, et al. Flexible, chemically bonded Bi–PVA–PVP composite for enhanced diagnostic X–ray shielding applications. J Inorg Organ Polym Mater 2023;33:2279–91. https://doi.org/10.1007/s10904-023-02662-4.

[11] Kavgacı M, Eskalen H. Morphology, structure and optical properties of PVA nanocomposites reinforced with bismuth oxide nanoparticles and carbon quantum dots. J Mater Sci Mater Electron 2023;34:1229. https://doi.org/10.1007/s10854-023-10617-1.

[12] Badawi A. Engineering the optical properties of PVA/PVP polymeric blend in situ using tin sulfide for optoelectronics. Appl Phys A 2020;126:335. https://doi.org/10.1007/s00339-020-03514-5.

[13] Badawi A, Mersal GAM, Shaltout AA, Boman J, Alsawat M, Amin MA. Exploring the structural and optical properties of FeS filled graphene/PVA blend for environmental-friendly applications. J Polym Res 2021;28:270. https://doi.org/10.1007/s10965-021-02626-7.

[14] Badawi A, Alharthi SS, Alotaibi AA, Althobaiti MG. Investigation of the mechanical and electrical properties of SnS filled PVP/PVA polymeric composite blends. J Polym Res 2021;28:205. https://doi.org/10.1007/s10965-021-02569-z.

[15] Alharthi SS, Badawi A. Tailoring the linear and nonlinear optical characteristics of PVA/PVP polymeric blend using $Co_{0.9}Cu_{0.1}S$ nanoparticles for optical and photonic applications. Opt Mater 2022;127:112255. https://doi.org/10.1016/j.optmat.2022.112255.

[16] Tiamduangtawan P, Kamkaew C, Kuntonwatchara S, Wimolmala E, Saenboonruang K. Comparative mechanical, self-healing, and gamma attenuation properties of PVA hydrogels containing either nano- or micro-sized Bi_2O_3 for use as gamma-shielding materials. Rad Phys Chem 2020;177:109164. https://doi.org/10.1016/j.radphyschem.2020.109164.

[17] Eyssa HM, Sadek RF, Mohamed WS, Ramadan W. Structure-property behavior of polyethylene nanocomposites containing Bi_2O_3 and WO_3 as an eco-friendly additive for radiation shielding. Ceram Int 2023;49:18442–54. https://doi.org/10.1016/j.ceramint.2023.02.216.

[18] Ahamed M, Akhtar MJ, Khan MAM, Alaizeri ZM, Alhadlaq H. Facile synthesis of Zn-doped Bi_2O_3 nanoparticles and their selective cytotoxicity toward cancer cells. ACS Omega 2021;6:17353–61. https://doi.org/10.1021/acsomega.1c01467.

[19] Karaca E. Electrosynthesis of binder-free polypyrrole/nano- Bi_2O_3-$Bi_2O_2CO_3$ composite for supercapacitor anode. J Energy Storage 2023;71:108210. https://doi.org/10.1016/j.est.2023.108210.

[20] El Askary A, Awwad NS, Ibrahium HA, Moustapha ME, Menazea AA. Structural, thermal, morphological and antibacterial activities of hybrid bio-nanocomposite Chitosan/Au/Bi2O3 for biomedical applications. J Polym Res 2022;29:269. https://doi.org/10.1007/s10965-022-03116-0.

[21] El-Sharkawy RM, Abdou FS, Gizawy MA, Allam EA, Mahmoud ME. Bismuth oxide nanoparticles (Bi2O3 NPs) embedded into recycled- Poly (vinyl chloride) plastic sheets as a promising shielding material for gamma radiation. Rad Phys Chem 2023;208:110838. https://doi.org/10.1016/j.radphyschem.2023.110838.

[22] Muthamma MV, Prabhu S, Bubbly SG, Gudennavar SB. Micro and nano Bi2O3 filled epoxy composites: thermal, mechanical and γ-ray attenuation properties. Appl Rad Isotop 2021;174:109780. https://doi.org/10.1016/j.apradiso.2021.109780.

[23] Mahmoud WE, Al-Ghamdi AA. Electrical and mechanical properties of bismuth oxide nanowire/poly(vinyl acetate). J Appl Polym Sci 2010;118:1598–605. https://doi.org/10.1002/app.32523.

[24] Du X, Liu Y, Wang X, Feng J, Ren C. Rapid preparation of α, β-Bi2O3 and α/β-Bi2O3 heterojunction with enhanced photocatalytic properties. J Austral Ceram Soc 2019;55:71–6. https://doi.org/10.1007/s41779-018-0212-5.

[25] Choudhary AR, Waghuley SA. In situ Bi_2O_3-loaded polypyrrole nanocomposites for carbon dioxide gas sensing. Iran Polym J 2019;28:933–41. https://doi.org/10.1007/s13726-019-00754-y.

[26] Gholamzadeh L, Mehrjardi AZ. Bismuth (III) oxide (Bi2O3)/poly (vinyl alcohol) nanocomposite fiber-coated polyester fabrics for multifunctional applications. Clean Techn Environ Policy 2023. https://doi.org/10.1007/s10098-023-02533-z.

[27] Nunez-Briones AG, Benavides R, Bolaina-Lorenzo ED, Martínez-Pardo ME, Kotzian-Pereira-Benavides C, Puente-Urbina BA, García-Cerda LA. Effect of Bi_2O_3 nanostructures on X-ray shielding, thermal, mechanical and biological properties of PVC polymer nanocomposites. Rad Phys Chem 2024;216:111455. https://doi.org/10.1016/j.radphyschem.2023.111455.

[28] Şahin N, Beyazay E, Karabul Y, Kılıç M, Esmer K, Özdemir ZG. LDPE/Bi_2O_3 nanocomposites: enhanced mechanical, dielectric, and optical properties. J Appl Polym Sci 2024;141:e55126.

[29] Tommalieh MJ. Electrical conductivity characterization of Chitosan/Poly (vinyl alcohol) doped by bismuth oxide nanoparticles. Compos Commun 2021;25:100692. https://doi.org/10.1016/j.coco.2021.100692.

[30] Darwesh AHA, Aziz SB, Hussen SA. Insights into optical band gap identification in polymer composite films based on PVA with enhanced optical properties: Structural and optical characteristics. Opt Mater 2022;133:113007. https://doi.org/10.1016/j.optmat.2022.113007.

[31] Mohammed Gh, El Sayed AM, Morsi WM. Spectroscopic, thermal and electrical properties of MgO/PVP/PVA nanocomposites. J Phys Chem Solids 2018;115:238–47. https://doi.org/10.1016/j.jpcs.2017.12.050.

[32] El Sayed AM, Mohamed ADM. Synthesis, structural, thermal, optical and dielectric properties of chitosan biopolymer; influence of PVP and α-Fe_2O_3 nanorods. J Polym Res 2018;25:175. https://doi.org/10.1007/s10965-018-1571-x.

[33] Shash NM, Khoder H, Metawe F, Negm AA. Structure, electrical, dielectric, and optical investigation on polyvinyl alcohol/metal chloride nanocomposites. J Appl Polym Sci 2013;129(5):2796–805. https://doi.org/10.1002/app.38998.

[34] Shamekh AMA, Shaalan NM, Hanafy TA, Rashad M. Linear/nonlinear optical properties of functional inorganic MgO nano-filler in PVA transparent polymer for flexible optoelectronic devices. Phys B 2023;651:414617. https://doi.org/10.1016/j.physb.2022.414617.

[35] El Gohary HG, Asnag GM, Tarabiah AE, Qahtan TF, Abdelrazek EM, Cevik E, et al. Modification and development of optical, thermal, dielectric properties and antibacterial activity of PVA/SA blend by Ag/Se nanofillers: nanocomposites for energy storage devices and food packaging applications. Polym Test 2023;129:108258. https://doi.org/10.1016/j.polymertesting.2023.108258.

[36] Alzahrani HS, Al-Sulami AI, Alsulami QA, Rajeh A. A systematic study of structural, conductivity, linear, and nonlinear optical properties of PEO/PVA-MWCNTs/ZnO nanocomposites films for optoelectronic applications. Opt Mater 2022;133:112900. https://doi.org/10.1016/j.optmat.2022.112900.

[37] El Sayed AM. Synthesis, optical, thermal, electric properties and impedance spectroscopy studies on P(VC-MMA) of optimized thickness and reinforced with MWCNTs. Res Phys 2020;17:103025. https://doi.org/10.1016/j.rinp.2020.103025.

[38] Alves R, Sentanin F, Sabadini RC, Pawlicka A, Silva MM. Green polymer electrolytes of chitosan doped with erbium triflate. J Non-Crystall Solids 2018;482:183–91. https://doi.org/10.1016/j.jnoncrysol.2017.12.038.

[39] Alanazi TI, El Sayed AM. M3+/NaTiO3/PVA–Chitosan nanocomposites (M = Ga, Ce, Nd or Er): novel solid polymer electrolytes for supercapacitors. Phys Scr 2023;98:085946. https://doi.org/10.1088/1402-4896/ace85d.

[40] Ji X, Wang W, Duan J, Zhao X, Wang L, Wang Y, et al. Developing wide pH-responsive, self-healing, and anti-corrosion epoxy composite coatings based on encapsulating oleic acid/ 2-mercaptobenzimidazole corrosion inhibitors in chitosan/poly(vinyl alcohol) core-shell nanofibers. Prog Org Coat 2021;161:106454. https://doi.org/10.1016/j.porgcoat.2021.106454.

[41] Bharati DC, Rawat P, Saroj AL. Structural, thermal, and ion dynamics studies of PVA-CS-NaI-based biopolymer electrolyte films. J Solid State Electrochem 2021;25:1727–41. https://doi.org/10.1007/s10008-021-04946-6.

[42] Liu Q, Chen Q, Tang Y, Cheng H-M. Interfacial modification, electrode/solid-electrolyte engineering, and monolithic construction of solid-state batteries. Electrochem Energy Rev 2023;6:15. https://doi.org/10.1007/s41918-022-00167-1.

[43] Thomas D, Zhuravlev E, Wurm A, Schick C, Cebe P. Fundamental thermal properties of polyvinyl alcohol by fast scanning calorimetry. Polymer 2018;137:145–55. https://doi.org/10.1016/j.polymer.2018.01.004.

[44] Xia X, Li J, Zhang J, Weng GJ. Uncovering the glass-transition temperature and temperature-dependent storage modulus of graphene-polymer nanocomposites through irreversible thermodynamic processes. Int J Eng Sci 2021;158:103411. https://doi.org/10.1016/j.ijengsci.2020.103411.

[45] El Sayed AM, Morsi WM. Dielectric relaxation and optical properties of polyvinyl chloride/lead monoxide nanocomposites. Polym Compos 2013;34:2031–9. https://doi.org/10.1002/pc.22611.

[46] Fahmy T, Elhendawi H, Elsharkawy WB, Reicha FM. AC conductivity and dielectric relaxation of chitosan/poly(vinyl alcohol) biopolymer polyblend. Bull Mater Sci 2020;43:243. https://doi.org/10.1007/s12034-020-02207-2.

[47] El-Sayed S, Abdel-Baset TA, Hassen A. Dielectric properties of PVDF thin films doped with 3 wt.% of RCl3 (R = Gd or Er). AIP Adv 2014;4:037114. https://doi.org/10.1063/1.4869093.

[48] Mohammed Gh, El Sayed AM. Structural, morphological, optical and dielectric properties of M3+/PVA/PEG SPE Films (M = La, Y, Fe or Ir). Polym Adv Technol 2019;30:698–712. https://doi.org/10.1002/pat.4508.

[49] Meera K, Ramesan MT. Tailoring the performance of boehmite nanoparticles reinforced carboxymethyl chitosan/cashew gum blend nanocomposites via green synthesis. Polymer 2023;268:125706. https://doi.org/10.1016/j.polymer.2023.125706.

[50] Alsulami QA, Rajeh A. Synthesis of the SWCNTs/TiO_2 nanostructure and its effect study on the thermal, optical, and conductivity properties of the CMC/PEO blend. Res Phys 2021;28:104675. https://doi.org/10.1016/j.rinp.2021.104675.

[51] El Sayed AM. Aspects of structural, optical properties, and relaxation in (BiFeO3 or NaTiO3)–PMMA: hybrid films for dielectric applications. J Phys Chem Solids 2021;148:109767. https://doi.org/10.1016/j.jpcs.2020.109767.

[52] Mishra MK, Moharana S, Behera B, Mahaling RN. Surface functionalization of BiFeO3: a pathway for the enhancement of dielectric and electrical properties of poly(methyl methacrylate)–BiFeO3 composite films. Front Mater Sci 2017;11(1):82–91. https://doi.org/10.1007/s11706-017-0364-1.

[53] Badawi A, Alharthi SS, Althobaiti MG, Alharbi AN. The effect of iron oxide content on the structural and optical parameters of polyvinyl alcohol/graphene nanocomposite films. J Vinyl Addit Technol 2022;28:235–46. https://doi.org/10.1002/vnl.21889.

[54] Abed RN, Zainulabdeen K, Abdallh M, Yousif E, Rashad AA, Jawad AH. The optical properties behavior of modify poly(methyl methacrylate) nanocomposite thin films during solar energy absorption. J Non-Crystall Solids 2023;609:122257. https://doi.org/10.1016/j.jnoncrysol.2023.122257.

[55] Yang S, Wang L, Yue S, Lu Y, He J, Zhao D. Influence of reduction temperature on composition, particle size, and magnetic properties of CoFe alloy nanomaterials derived from layereddouble hydroxides precursors. Dalton Trans 2014;43:8254–60. https://doi.org/10.1039/C4DT00137K.

[56] Mohamed MB, Abdel-Kader MH. Effect of excess oxygen content within different nano-oxide additives on the structural and optical properties of PVA/PEG blend. Appl Phys A 2019;125:209. https://doi.org/10.1007/s00339-019-2492-1.

[57] Hadi A, Hashim A, Al-Khafaji Y. Structural, optical and electrical properties of PVA/PEO/SnO_2 new nanocomposites for flexible devices. Transact Electr Electron Mater 2020;21:283–92. https://doi.org/10.1007/s42341-020-00189-w.